

DYNAMICAL EXCITATION AS A PROBE OF PLANETARY ORIGINS

BRAD M. S. HANSEN

Mani L. Bhaumik Institute for Theoretical Physics, Department of Physics & Astronomy, University of California Los Angeles, Los Angeles, CA 90095

TZE-YEUNG YU

Mani L. Bhaumik Institute for Theoretical Physics, Department of Physics & Astronomy, University of California Los Angeles, Los Angeles, CA 90095

NEEL NAGARAJAN

Mani L. Bhaumik Institute for Theoretical Physics, Department of Physics & Astronomy, University of California Los Angeles, Los Angeles, CA 90095

YASUHIRO HASEGAWA

Jet Propulsion Laboratory, California Institute of Technology, Pasadena, CA, 91109

Version October 3, 2025

ABSTRACT

We present a set of numerical simulations of the dynamical evolution of compact planetary systems migrating in a protoplanetary disk whose inner edge is sculpted by the interaction with the stellar magnetic field, as described in Yu et al. (2023). We demonstrate that the resulting final distribution of neighbouring planet period ratios contains only a small surviving fraction of resonant systems, in accordance with observations. The resulting planetary architectures are largely in place by the end of the protoplanetary disk phase (within a few Myr), and do not require significant later dynamical evolution.

The divergence of planetary pairs during gas disk dispersal also leads to the excitation of eccentricities when pairs cross mean motion resonances in a divergent fashion. The resulting distribution of remnant free eccentricities is consistent with the values inferred from the observation of transit durations and transit timing variations. We furthermore demonstrate that this conclusion is not significantly altered by tides, assuming standard values for tidal dissipation in Earth or Neptune-class planets.

These results demonstrate that the observed spacing and residual dynamical excitation of compact planetary systems can be reproduced by migration through a protoplanetary disk, as long as the inner disk boundary is modelled as a gradual rollover, instead of a sharp transition. Such an effect can be achieved when the model accounts for the diffusion of the stellar magnetic field into the disk. The resulting divergence of planetary pairs during the magnetosospheric rebound phase breaks the resonant chains, resulting in a better match to observations than disk models with more traditional inner boundaries.

1. INTRODUCTION

The ongoing census of extrasolar planetary systems has revealed that the most common planetary systems orbiting Solar-like stars contain multiple planets in the Earth–Neptune mass range, arrayed in compact configurations with orbital periods that frequently lie well within that of Mercury in our Solar system (Borucki et al. 2010; Batalha et al. 2013; Fressin et al. 2013; Petigura et al. 2013; Coughlin et al. 2016; Lissauer et al. 2023). Despite their widespread occurrence, the origins of these planets is still a matter of lively debate.

One school of thought suggests that such planets, especially those with volatile-rich envelopes, formed fur-

ther from the star and migrated inwards due to interactions with the gaseous protoplanetary disk. The migration timescales associated with low mass planets are quite short, but gravitational interactions between multiple migrating planets can slow the evolution sufficiently to avoid losing the planets into the central star (Terquem & Papaloizou 2007; Ida & Lin 2008, 2010; Hellary & Nelson 2012; Cossou et al. 2014; Coleman & Nelson 2014; Izidoro et al. 2017). The observed high frequency of multiple planet systems also aligns nicely with this model. However, such models predict a high occurrence rate of mean motion resonances in such systems Masset & Snellgrove (2001); Cresswell & Nelson (2006); Mustill & Wyatt (2011), which is not matched by observations (Lissauer et al. 2011; Fabrycky et al. 2014).

An alternative class of models suggests that the planets assembled *in situ*, with little radial migration (Hansen & Murray 2012; Chiang & Laughlin 2013; Boley et al. 2014; Chatterjee & Tan 2015; Poon et al. 2020). These models can better match the observed spacing of planets in multiple systems (Hansen & Murray 2013), but require that the protoplanetary disks be either unusually massive or allow for significant inward migration of solid material as small bodies, prior to assembly.

These two models represent two conceptual extremes, and recent work has explored scenarios which lie somewhat in between. The resonant chains produced by migration may be broken by additional perturbations, such as from scattering by remnant planetesimals (Chatterjee & Ford 2015; Ghosh & Chatterjee 2023; Wu et al. 2024), late time mass loss (Matsumoto & Ogihara 2020) and excitation from distant giant planets (Li et al. 2014; Hands & Alexander 2016; Hansen 2017; Huang et al. 2017; Becker & Adams 2017; Mustill et al. 2017; Pu & Lai 2019; Denham et al. 2019; Poon & Nelson 2020; Pu & Lai 2021). The simple resonant chain model may also be modified by more detailed migration models. At late times, as the accretion rate drops, the magnetospheric cavity will expand, and the evolution of the torques during this ‘magnetospheric rebound’ can destabilise some resonances (Liu et al. 2017). Izidoro et al. (2021) consider a model in which migration occurs during the assembly process, with migrating embryos growing through the accretion of both planetesimals and planets. This leads to an inner planetary system composed of dense, resonant, chains of low mass planets that become dynamically unstable after the disk dissipates, leaving behind final systems with a higher probability of being non-resonant. Hansen et al. (2024) consider a model in which the migration occurs in a disk with an inner edge sculpted by the interaction with a stellar magnetic field, as described in Yu et al. (2023). During the magnetospheric rebound phase, as the disk dissipates, the evolution of this inner edge leads to resonant divergence and, once again, disruption of most of the original chains.

A variety of statistics have been used to quantify the comparison between these models and observations, including the distribution of nearest neighbour period ratios, distribution of final planetary masses and orbital periods, relative frequency of multiple transit systems, and a variety of measures designed to quantify the statistical properties of planetary systems (Laskar 1997; Chambers 2001; Gilbert & Fabrycky 2020; Goldberg & Batygin 2022; Shariat et al. 2024).

Of particular interest is the distribution of residual orbital eccentricities. The most straightforward migration models predict very low eccentricities due to the eccentricity damping by the gas disk. In the case of *in situ* assembly models, very few systems are ever in resonance, and the eccentricity distribution is a remnant of the scattering during the assembly process (Hansen & Murray 2013; Dawson et al. 2016). We expect the more sophisticated migration models to lie somewhere in between, because there needs to be a mechanism to break the chains after they have been formed, and the eccentricities will provide a probe of the resulting excitation (Izidoro et al. 2017; Goldberg & Batygin 2022). Measuring the level of residual dynamical excitation in planetary systems is therefore potentially a powerful discriminant

between different origin scenarios.

As a first step in this direction, we present here a full dynamical simulation of the migration scenario outlined in Yu et al. (2023) and Hansen et al. (2024). This describes migration of planets within a protoplanetary disk with a physically motivated inner edge, maintained by the interaction with the stellar magnetic field. The distinguishing feature of this model is the presence of a transition zone between the inner edge and a location where the disk torque reverses direction, so that planets pushed inwards of the torque reversal experience outwardly-directed migration. During the later stages of the disk lifetime – as the magnetospheric cavity expands – this leads to divergent evolution, and the breaking of many resonant chains. The result is a period-ratio distribution much more consistent with observations than other migration models, and without invoking late-time dynamical instabilities. Many pairs also experience temporary excitation of eccentricity during these late stages, when their divergent evolution passes through a mean motion resonance. This can potentially explain the puzzling persistence of small levels of free eccentricity in many of these systems (Hadden & Lithwick 2014, 2017), and so we wish to explore, in some detail, how the residual level of eccentricity in these systems can be used to probe planetary origins.

In § 2 we describe our dynamical simulations of the planetary scenario described in Yu et al. (2023) and Hansen et al. (2024), and explore the dynamical mechanisms that lead to the final levels of eccentricity excitation. Tidal dissipation can reduce the observable eccentricity so, in § 3 we explore the role played by tidal evolution in these systems. In § 4 we compare these results to known observational constraints.

2. DYNAMICAL MODEL

Yu et al. (2023) presents a model of a protoplanetary disk, incorporating both viscous and radiative heating, in which low mass planets migrate inwards due to the Type I migration torque formulae from Hellary & Nelson (2012). The models also incorporate a disk inner edge sculpted by the diffusion of the stellar magnetic field into the disk. The effective viscosity near the inner edge is increased as a result of the stellar field torques, resulting in a peak of the surface density at a location exterior to the inner edge (the nominal magnetospheric cavity). This causes a reversal of the migration torque at the surface density peak, and a change in the direction of planetary migration before the planet reaches the true disk inner edge. The resulting influence of this torque behaviour, and its evolution over time, was studied in Hansen et al. (2024). Most simulated systems initially formed a chain of resonant pairs during inward migration – a result consistent with other migration models. However, as the accretion rate drops, the location of the torque reversal moves outwards during the magnetospheric rebound phase. At this point, many of the migrated planets lay interior to the torque reversal, and so many planet pairs experienced divergent migration at late times. This resulted in most of the original resonant chains being broken during the dissolution of the protoplanetary disk.

The simulations of Hansen et al. (2024) were based on a semi-analytic model that included only the three lowest first order resonances. This was sufficient to demonstrate

the most important feature of the model – namely that it produced a population of planets with a low resonant fraction, as observed. However, our goal in this paper is to extend this study to quantify the level of residual dynamical excitation in these model systems. To do this properly, we wish to include the full range of gravitational interactions between the planets in each system. Therefore, we have simulated planetary migration and dynamical evolution following the same setup as in Hansen et al. (2024), but now using the *Mercury* integrator (Chambers 1999) to follow the full dynamical evolution. In addition to the direct calculation of gravitational interaction between all bodies in the system, the planets are subject to the same gaseous torques as described in Hansen et al. (2024), following the underlying disk model. We use the same disk torques model described in equations (1)–(4) in Hansen et al. (2024), which is based on the $B_0 = 1.7\text{kG}$ and $n = 3.5$ model from Yu et al. (2023).

For the selection of planetary initial conditions, we follow the model of § 5.2 of Hansen et al. (2024). Masses for each system represent a particular Kepler analogue, with a mass model based on the observed radii and the mass–radius relationship from Chen & Kipping (2018). This approach means that our model should contain the same range of masses and neighbor mass ratios as the observed Kepler systems (although the final period ratios may differ from the corresponding observed system, depending on the migration model and the probabilistic nature of resonant capture). The initial semi-major axis for the innermost planet is 0.08 AU and the starting semi-major axis for each additional planet is a factor 1.5 larger than the inner neighbour. This ensures that all planet pairs start with period ratios between the 3:2 and 2:1 resonances. It is likely that the planets assembled further out and migrated inwards, but Hansen et al. (2024) demonstrated that the memories of the initial conditions are lost once the system enters a resonance lock, so we have focussed our computational resources on the approach to resonance capture and later divergence. Initial eccentricities are set to 0.1 and initial inclinations are chosen with a dispersion of 0.1° . The initial values of the argument of perihelion, the line of nodes, and the mean anomaly are all given a random value between 0 and 360° . As a result of the dissipative forces we have added to the dynamics, we use the Bulirsch–Stoer integrator in *Mercury*, with a default timestep of 6 hours (because many of our systems ultimately evolve to short orbital periods).

2.1. Two Planet Systems

The migration of individual planets in this model are driven entirely by the gas torques and closely follow the same evolutionary path as described in Yu et al. (2023). The evolution of two planet systems does incorporate mutual gravitational interactions, and we have simulated planetary pairs with masses chosen using the above procedure. Once again, the semi-analytic models, in this case, Hansen et al. (2024) capture the dynamics accurately. Most importantly, for the purposes of this paper, we observe eccentricity excitation when pairs cross a mean motion resonance in the latter stages of the disk evolution. At late times, during the dispersal of the disk, the torque reversal location is moving outwards, and many planetary pairs are diverging. The crossing

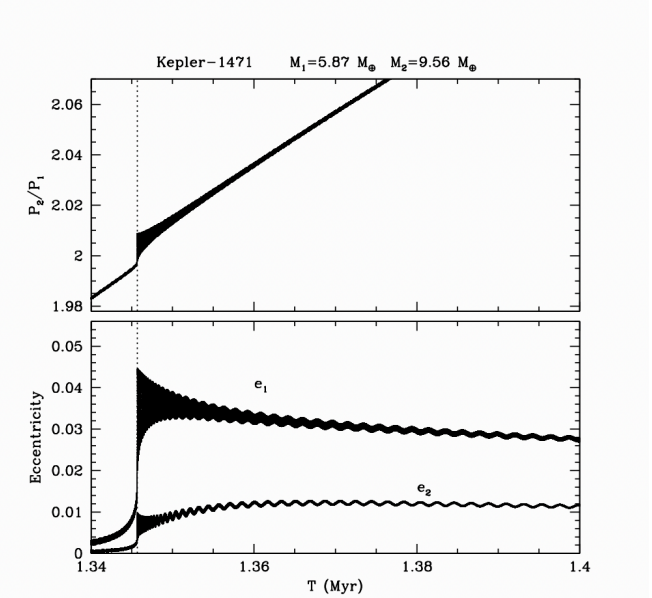


FIG. 1.— The upper panel shows the evolution of the period ratio of the planetary pair in the system modelled after Kepler-1471. The jump at age 1.345 Myr is the divergence crossing of the 2:1 resonance. In the lower panel, we see a corresponding spike in the eccentricity of both planets, most of which remains after the disk has finally dispersed.

of a resonance (in most cases studied here, the 2:1 mean motion resonance) results in a transient eccentricity excitation. Once the pair has passed through the resonance, the eccentricities begin to damp again. However, many of these divergent crossings occur late in the disk dispersal and the damping is incomplete, leaving a residual eccentricity in the system.

Figure 1 shows an example of this, that occurs in our analog of the Kepler-1471 system. The inner planet has a mass of $5.87 M_\oplus$ and the outer planet has a mass of $9.56 M_\oplus$. This pair initially captures into the 3:2 mean motion resonance, during its inward migration. Since, the outer planet is more massive, it remains coupled to the disk for longer during the magnetospheric rebound phase, and the resulting diverging pair eventually crosses the 2:1 resonance at 1.34 Myr. Both planets receive a spike in the eccentricity during this passage. The pair eventually freezes out at a period ratio $P_2/P_1 = 2.28$, with eccentricities $e_1 = 0.022$ and $e_2 = 0.009$. As noted by Lin et al. (2024), such divergent resonance crossings have the potential to dictate the final residual eccentricities exhibited by transiting planets. We will examine the population-level consequences of this in § 2.6.

The final level of eccentricity excitation is a function of the planetary mass ratio, as is shown in Figure 2. Systems in which the planets have mass ratios close to or slightly below unity do not show a large amount of eccentricity. This is because both planets decouple from the disk at about the same time, and so there is not sufficient differential movement in semi-major axis to cause the system to break the original resonance lock and then evolve to the point where they cross another resonance. For systems with $M_2 > M_1$, the outer planet moves far enough to generate such a divergent crossing (as in Fig-

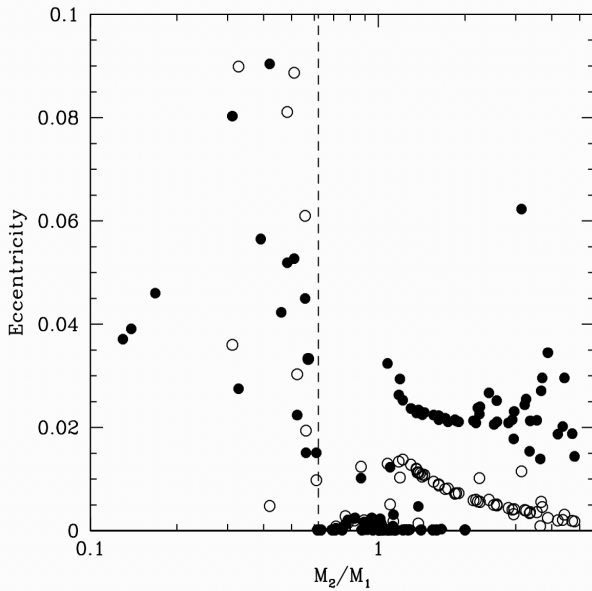


FIG. 2.— The solid points show the inner planet eccentricity after 2 Myr, while the open circles show the outer planet eccentricity. The distribution of eccentricities as a function of planetary mass ratio breaks up into three regimes. To the left of the vertical dashed line, i.e. at small M_2/M_1 , all systems remain in resonance to the end of the simulation. Thus, the eccentricities are determined by the resonant lock of the pair. For mass ratios around unity, the final eccentricities are small, because the pairs break out of resonance and damp eccentricity. On the right, the eccentricities are large again because the pairs diverge far enough to cross another mean motion resonance, resulting in late-time eccentricity excitation that persists to the end of the simulation.

ure 1), resulting in the remnant eccentricities shown on the right of Figure 2. For systems with $M_2/M_1 < 0.6$, it is the inner planet that remains coupled to the disk for longer and so the outer planet will get swept along and remain in resonance. The larger eccentricities on the left of the vertical dashed line in Figure 2 are therefore a consequence of maintaining the resonant lock to the end of the simulation.

2.2. Triple Planet Systems

The two planet systems follow the semi-analytic evolution of Hansen et al. (2024) quite closely. However, systems with more planets can potentially introduce significantly more dynamical complexity. The migration rate is a function of both mass and semi-major axis, so individual pairs may converge or diverge, depending on their parameters. The interaction between these pairs can introduce effects not treated in the semi-analytic models.

An example is shown in Figure 3, a system with masses motivated by the triple planet system Kepler-295. As in the semi-analytic models, the innermost planet is the first to encounter the torque reversal and therefore halt its inward migration. The second and third planets quickly lock into a 2:1+2:1 chain of mean motion resonances, driving the innermost planet interior to the torque reversal location. However, the disk torques are strong enough to drive the planets closer together, resulting in a cascade down through resonances until a 4:3+5:4 chain is created, which reaches a relatively stable configuration once the third planet reaches the torque reversal. The system re-

mains in this resonant configuration as the torque reversal begins to move outwards. Although all three planets are, at this point, migrating outwards rather than inwards, their resonant lock is maintained by the fact that their relative outward migration rates still yield convergent evolution.

At late times, the outward evolution accelerates as the disk surface density drops, and the planetary migration rates cannot keep up. As the planet migration decouples from the disk evolution, the pairs can no longer maintain the converging relative motion, and the pairs drop out of resonance. The resonant chains are broken, so that the final period ratios are not in resonance (nor is the trio in a three-body resonance).

As long as the pairs remain in resonance, the eccentricities are maintained by the resonant lock (Terquem & Papaloizou 2019) in the face of the disk eccentricity damping. The lower right hand panel of Figure 3 shows that the equilibrium eccentricity values shift at each change in the resonance configuration, as the signs of the torques driving the migration change. This holds even during the outward migration, as long as the pairs are still converging, but the eccentricities drop rapidly once the pairs leave resonance. Figure 3 also shows that the divergence can be far enough to allow pairs to cross multiple resonances in a divergent fashion. In the case shown here, we see that the outer pair diverges from the original 5:4 commensurability and passes through the 4:3 and 3:2 resonances at late times, resulting in a spike in the eccentricity during each divergent crossing. This can be observed in the lower right panel of Figure 3, and leaves the system with a low level of finite eccentricity at late times. This is an essential contribution to the final level of dynamical excitation, and will be explored further in § 2.6.

However, not every system breaks the resonant chain. Figure 4 shows the evolution of a three planet system whose masses are based on those of the triple planet Kepler-295 system, and which remains in the resonant chain after the end of the disk phase. This is one of the more massive systems in our simulation set, with all the planets $> 10M_\oplus$. The strength of the disk torque scales with mass, so more massive planets remain coupled to the gas disk for longer. Furthermore, the most massive planet in this system is the innermost one, so it will continue to move outwards longest, and maintain the convergent nature of the innermost pair, even as both planets move outwards.

A further interesting feature of this system is that the resonant angles of the inner pair do not librate about 0 and π , but rather about some intermediate values. These are examples of the ‘asymmetric equilibria’ of three-body resonant chains, discussed by Wang et al. (2024) (see also Delisle (2017)). They can be heuristically understood as a consequence that planets in a chain of resonances are subjected to driving from multiple oscillators, leading to equilibria that cannot be found in the two planet case. It is worth noting that the corresponding three-body resonant angle also has a different libration center. As the disk dissipates and the driving torques decrease, these offsets are reduced, but they retain a non-zero difference at the end of the evolution.

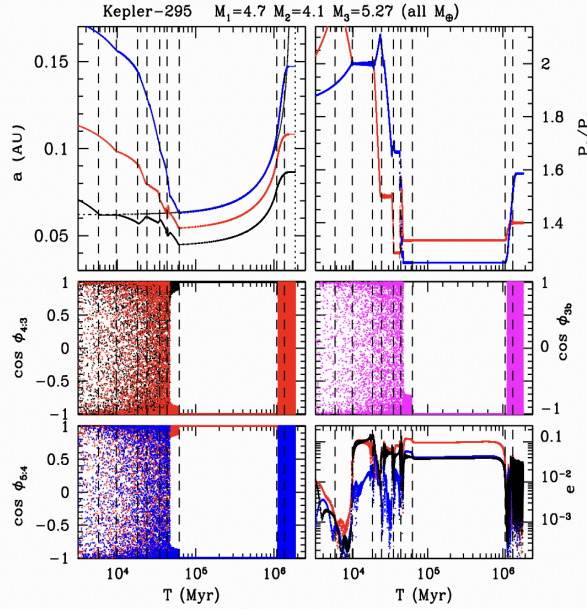


FIG. 3.— The upper left plot shows the evolution of the semi-major axes for a three planet system under the influence of the torques derived from the protoplanetary disk. The black curve represents the innermost planet, the red curve the middle planet and the blue curve the outer planet. The dotted line tracks the location of the torque reversal. Important transitions in the system properties are marked by vertical dashed lines. The right-hand plot shows the evolution of the nearest neighbour period ratios (color coded by the outer planet in each pair). The panel in the lower right shows the evolution of the eccentricity of each planet. The remaining panels show the evolution of different resonant angles. The two on the left show the two-body resonant angles for the outer pair (4:3) and inner pair (5:4), color-coded by the planetary precession term in the resonant argument. The magenta curve on the right shows the evolution of the three-body resonant angle. The system masses are in units of M_{\oplus} .

2.3. Higher Multiplicity Systems

Another advantage of a full N-body simulation is that one can include an arbitrarily large number of planets. As such, in addition to the three planet systems simulated in Hansen et al. (2024), we simulated mass distributions corresponding to the Kepler quadruple, quintuple and sextuple systems. This followed the same procedure as in Hansen et al. (2024), wherein the masses are a chosen from the probability distribution of Chen & Kipping (2018), estimated from the observed planetary radii, and we exclude systems with Jupiter-class ($R > 6R_{\oplus}$) planets. Figure 5 shows the evolution of a system whose masses were drawn from the distributions for the Kepler-80 system. The inner five planets of this system sequentially capture into a resonance chain of 3:2+2:1+3:2+2:1 over the first 10^5 years. This chain remains locked until an age $\sim 10^6$ years, before it too begins to fall apart as the planetary migration falls behind the disk evolution. The resonant angles in this chain also show a variety of symmetric and asymmetric equilibria. The first and third pairs librate in a traditional configuration, but the second and fourth pairs show libration about asymmetric equilibria. As the disk torques maintaining the resonant lock weaken, these equilibria evolve to more traditional libration centers, just before the resonances break and the eccentricities damp.

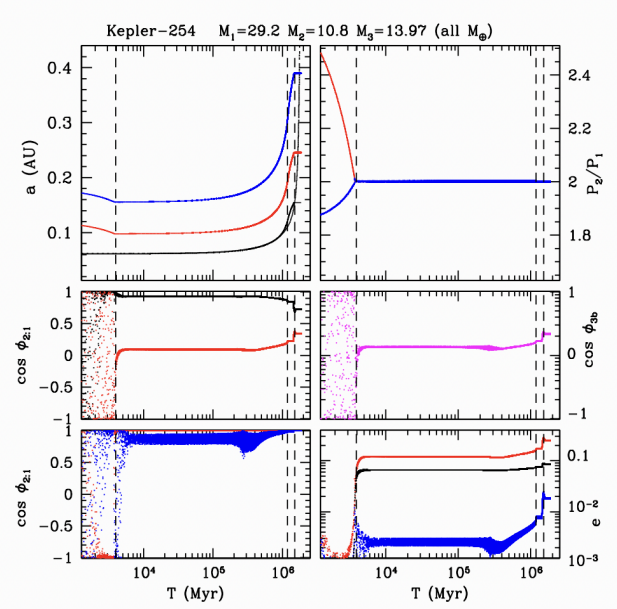


FIG. 4.— The upper left plot shows the evolution of the semi-major axes for a three planet system under the influence of the torques derived from the protoplanetary disk. The black curve represents the innermost planet, the red curve the middle planet and the blue curve the outer planet. Important transitions in the system properties are marked by vertical dashed lines. The dotted line tracks the location of the torque reversal. The right-hand plot shows the evolution of the nearest neighbour period ratios (color coded by the outer planet in each pair). The panel in the lower right shows the evolution of the eccentricity of each planet. The remaining panels show the evolution of different resonant angles. The two on the left show the two-body resonant angles for the outer pair (2:1) and inner pair (2:1), color-coded by the planetary precession term in the resonant argument. The magenta curve on the right shows the evolution of the three-body resonant angle. The system masses are in units of M_{\oplus} .

The outermost planet in the system takes a long time to migrate inwards (migration rates are slower further from the star) and only locks into the 2:1 resonance at late times (when the other planets have already broken their resonant locks). This lock is relatively brief, but it does leave some residual eccentricity excitation in the outermost planet. The inner planets are not strongly coupled to it and so receive only a limited eccentricity excitation.

2.4. Dynamical Instability

The bulk of our simulated systems evolve through the migration and rebound phase without undergoing any dynamical instabilities, but some do experience sufficient eccentricity excitation that some planets cross orbits and collide. We evolve these systems with *Mercury*, assuming perfect merging. An example of such a system is shown in Figure 6.

This shows a system of, initially, five planets, with masses chosen to represent Kepler-32. Figure 6 shows the five planet system evolving inwards in the standard fashion (with green curves showing the two planets that are eventually merged with others). The inner three planets settle into a stable configuration that tracks the torque reversal, while the outer two planets are still migrating inwards. When the fourth planet enters the resonant

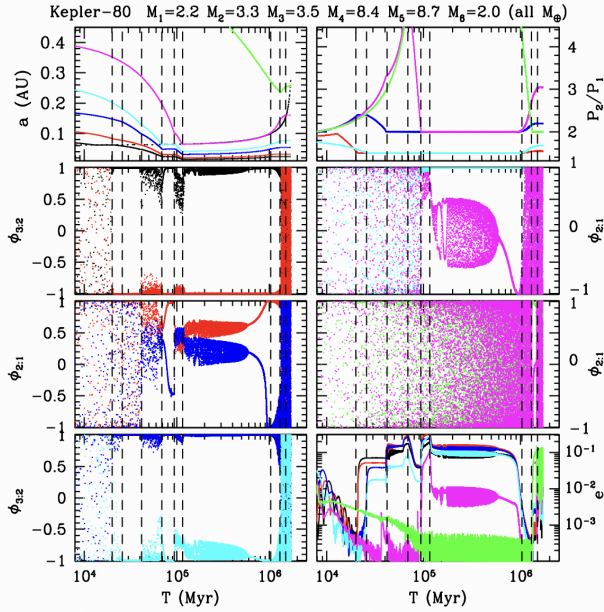


FIG. 5.— The upper panels show the evolution of the semi-major axes (left) and nearest neighbor period ratios (right) for a six planet migrating system. The panel in the lower right shows the corresponding evolution of the eccentricities. The other panels show the cosines of the most important resonant angle for each of the 5 nearest neighbour pairs, with the colours corresponding to the planets in the upper left panel. As before, the dotted line in the upper left shows the location of the torque reversal, and the vertical dashed lines indicate important epochs (when resonances are established or broken).

lock, it drives the interior planets inward, excites eccentricity and generates instability. This results in the merger of the inner pair ($\sim 6 \times 10^4$ years). The continued inward migration of the outermost planet (also the most massive in the system) soon results in an additional merger of the outer two planets (at $\sim 7 \times 10^4$ years).

The end result of this is a three planet system following the same outward evolution as we see in other systems, except for the unusual resonant configuration of 11:7+5:3. This also yields an unusual three-body resonant configuration of $10n_3 - 17n_2 + 7n_1 \sim 0$, as shown in Figure 6. As in other systems, this exotic resonant configuration is eventually disrupted by the outwards evolution, and the planets experience a similar late eccentricity kick due to divergent crossing of the 2:1 resonance at late times.

The overall fraction of systems that undergo dynamical instability increases with the multiplicity of the system. Of the original 107 triple systems simulated, 8 experienced dynamical instability and a planetary collision (a fraction of 7.5%). Of the original 39 quadruple systems, 11 experienced instability (28%), while 12/18 (67%) of high multiplicity systems experienced instability. Overall, 31/164 (19%) of simulated systems experienced instability.

2.5. Summary Statistics

As demonstrated in Hansen et al. (2024), the final period ratio distribution from this scenario is much more consistent with observations, without invoking any longer-term dynamical instabilities. Figure 7 shows the

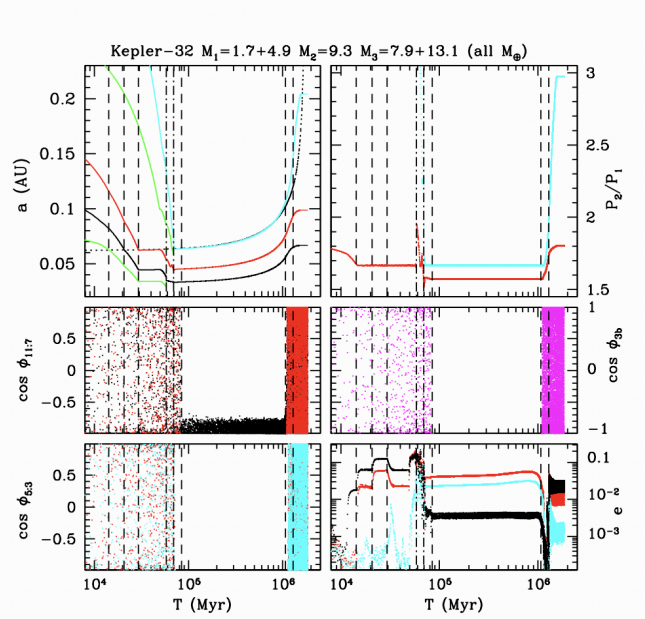


FIG. 6.— The upper panels show the evolution of the semi-major axes (left) and nearest neighbor period ratios (right) for a migrating system of (initially) five planets. In the upper left panel, the two green trajectories represent the two planets that are lost to merger with others. In the other panels, only trajectories of surviving planets are shown, coloured according to our previous convention, as applied to planets at the end. The panel in the lower right shows the evolution of the eccentricities. The other panels show the cosines of the most important resonant angle for each of the 5 nearest neighbour pairs, with the colours corresponding to the planets in the upper left panel. As before, the dotted line in the upper left shows the location of the torque reversal, and the vertical dashed lines indicate important epochs (when resonances are established or broken).

distribution of nearest neighbour period ratios derived from the full set of dynamical simulations of planetary systems of multiplicity three or higher. The ensemble of final configurations from our full set of simulations (all Kepler analogue mass systems for multiplicity three and above), is observed by randomly oriented observers, assuming that all planets that transit are detected (since our masses are derived directly from the Kepler sample, they are representative of the observed sample). Each system is weighted by the geometric probability of observing the innermost planet and then additional planets are weighted by the probability of observation relative to the innermost. The resulting sample is shown in the upper panel, and includes pairs where one or more intermediate planets are missed because they do not transit. The lower panel shows the observed sample of planets, in systems of three or more, from the final Kepler catalog (Thompson et al. 2018), selecting only those planets with orbital periods < 40 days. This is because our model only covers planets on these scales, and does not contain more distant planets.

The comparison of the upper and lower panels of Figure 7 indicate that the model broadly reproduces the observations, with a substantial population of pairs between the 3:2 and 2:1 resonances, and a tail extending to larger values (many of these represent pairs that actually have an nontransiting planet in between them). It is important to note that this emerges directly from

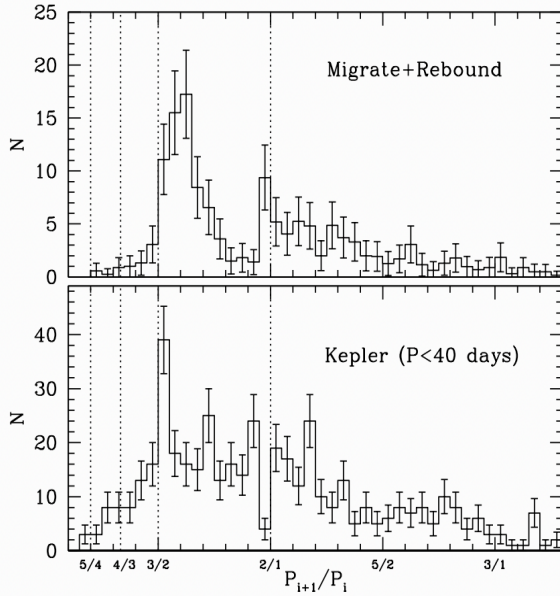


FIG. 7.— The panel shows the distribution of nearest neighbor period ratios from our simulations, when observed by randomly oriented observers. The lower panel shows the final observed Kepler satellite distribution, when restricted to orbital periods less than 40 days. Vertical dotted lines indicate the locations of the lowest four first order mean motion resonances.

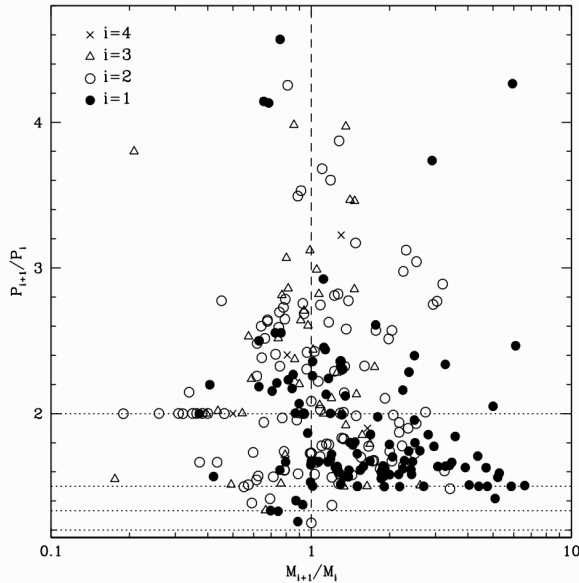


FIG. 8.— The filled circles show the period ratios versus mass ratios for the innermost pairs of multiplanet systems. The open circles show the ratios for the second and third innermost planets. The open triangles show the ratios for pairs containing the third and fourth innermost planets. These are fewer because they don't occur in three planet systems. Finally, the crosses indicate the pairs comprising the fourth and fifth planets in the systems. The horizontal dotted lines indicate the four lowest first order mean motion resonances and the vertical dashed line indicates mass equality.

the simulations, and does not require selective weighting of different subsamples of results, as is required to make

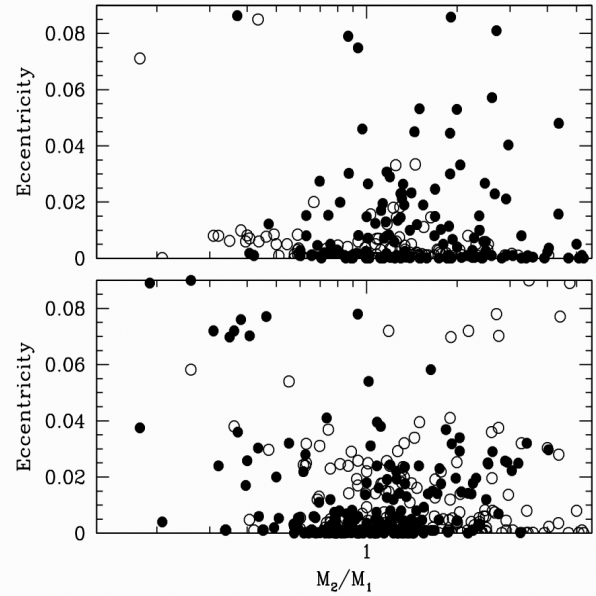


FIG. 9.— The solid points in the upper panel represent the eccentricity of the innermost planet in the higher multiplicity planetary systems (three or more), as a function of the inner pair mass ratio. The open points in the upper panel show the eccentricity of the outermost planet in each system, along with the mass ratio of the outermost pair. The lower panel shows the eccentricities of all other planets in these high multiplicity systems, against the mass ratio of both pairs to which they belong. Each eccentricity value appears twice in this plot – as a solid point when it is the inner member of a pair, and as an open point when it is the outermost member of a pair.

some other simulations match the data.

Closer examination of the structure around the 2:1 and 3:2 commensurabilities indicates that the agreement is not perfect, however. In particular, the model shows a symmetric structure around the 2:1 resonance, whereas the observations show a clear asymmetry. Similarly, the model peak around the 3:2 resonance is broader than that seen in the observed sample. Clearly, while the model does an excellent job of breaking most of the resonant chains, there are still some elements missing. We will discuss possible causes of this below.

As discussed in Hansen et al. (2024) and § 2.1, the mass ratio between neighbouring pairs is an important driver of when migration of pairs is divergent or convergent. Figure 8 shows the period ratios of neighboring pairs versus the mass ratio between the corresponding pairs. In this case, unlike Figure 7, only true neighbors are plotted (we do not account for transit probabilities here). Furthermore, the symbols are chosen to represent the position of each pair in the chain, because the presence of planets interior or exterior to a pair can affect the rate of convergence or divergence (gravitational interactions with these planets can impart an effective inertia).

The distribution of points in Figure 8 does explain the peak at the 2:1 resonance. This arises from pairs in which the inner planet is significantly more massive than the outer member. During the inward migration phase, the inner planets migrate faster and the pairs diverge beyond the 2:1 resonance. Once the inner planet reaches the torque reversal, the pair converges again and the pair

captures into the 2:1 resonance. This can be seen in the upper right panel of Figure 5. During the rebound phase, the inner planet remains coupled to the disk for longer, thereby maintaining the convergent migration and resonant lock through to the final decoupling of the planets from the disk. Our initial mass distribution was based on the observed Kepler masses, but the constraints were not very strict (Chen & Kipping 2017), so that one could reduce the size of the 2:1 peak in Figure 7 by restricting the mass ratios from being too small, or by enforcing initial conditions that favor capturing into closer resonances than 2:1. The peak at the 3:2 resonance, as well as the population just wide of it, is composed largely of inner pairs in which the outer member is more massive. In this instance, the outer planet remains coupled to the disk for longer, leading to divergence from resonance, which explains the large population from 1.5–1.8. Those that remain trapped in the peak are often slowed down by the presence of additional planets exterior to them. Indeed, the solid points in Figure 8 are clearly biased to smaller period ratios than the open points, indicating that their divergence is partially impeded by the gravitational interaction with the planets that lie further out in the planetary system.

As described in § 2.1, the mass ratio between neighbouring pairs of planets also has an effect on the residual eccentricities. Figure 9 shows the equivalent of Figure 2, but for pairs that are part of higher multiplicity systems. The upper panel shows the inner planet (solid points) and outer planet (open points) of each system, as they are only members of a single pair, and so this plot is most analogous to Figure 2. The lower panel shows the eccentricities of all the other planets in these systems. The eccentricities of these planets appear once as a solid point, and once as an open point, as each of these planets is a member of two pairs. We see that the division into three classes of eccentricity excitation as a function of mass ratio is much less clear here, a consequence of the greater variety of dynamical evolution that becomes possible with multiple planets interacting with each other and the disk torques.

2.6. Dynamical Excitation

Our goal is to examine the residual dynamical excitation in our simulations. This is shown in Figure 10, which shows the final eccentricities of each planet in a neighbouring pair in the models presented in Figure 8. This is plotted as a function of $|\Delta|$ – the distance to the nearest first order mean motion resonance, given by the commensurability $(q + 1)/q$. This is expressed as

$$\Delta = \frac{P_{i+1}/P_i}{(1 + q)/q} - 1 \quad (1)$$

Those for which $\Delta > 0$ are shown as a filled circle and those with $\Delta < 0$ as an open circle. The dotted curves indicate the libration amplitudes of the $q = 1, 2$ and 3 resonances for a $10M_{\oplus}$ planet, as given by equation (8.76) of Murray & Dermott (2000). Thus, points to the left of these curves are most likely still trapped in a resonant state, whereas those to the right are no longer resonant.

The pileup between the two vertical dashed lines is a consequence of the definition of Δ . Members of a pair that diverges from the 3:2 ($q=2$) resonance, for example,

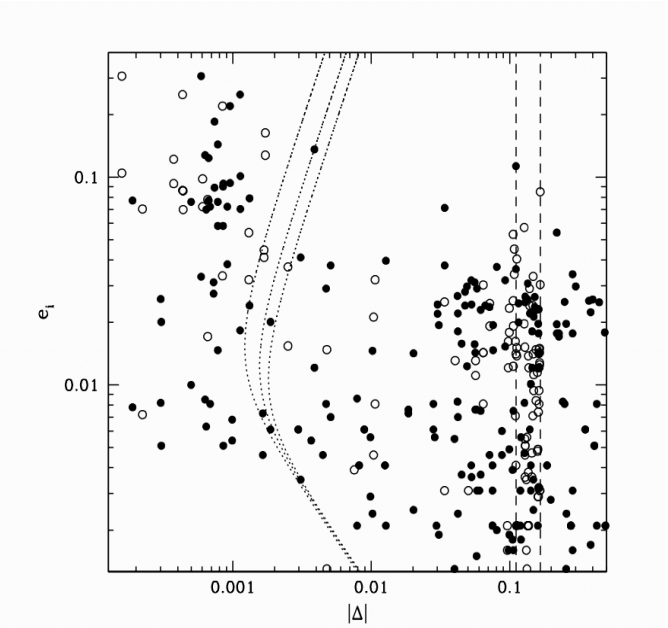


FIG. 10.— The filled circles are for $\Delta > 0$ and the open circles are for pairs with $\Delta < 0$. The dashed curves indicate the libration amplitudes for the first order resonances with $q=1, 2$ and 3 . The vertical dashed lines indicate the transition between proximity to the $q=2$ resonance and the $q=1$ resonance.

will move to the right in this diagram as a filled circle, until it reaches the first dashed line. Beyond this point (a period ratio of 5:3) it is closer to the $q=1$ commensurability than the $q=2$, and so jumps to the second dashed line. After this, it moves to the left, as an open circle, until it passes through the $q=1$ commensurability and again begins to move to the right as a filled circle.

The points to the left of the dotted lines in Figure 10 demonstrate that the resonant lock of some pairs will survive the late divergent migration, and that these represent the systems with the largest remnant eccentricities (~ 0.1). These values are imposed during the migration – a consequence of maintaining resonance lock during migration (Terquem & Papaloizou 2019). The values will evolve as the disk torques decrease, but the resonant libration will maintain them at non-zero levels in the face of the damping by the protoplanetary disk (which eventually goes away). The population to the right of the dotted lines represent pairs that have experienced divergent migration away from resonance, so that the eccentricities should have been damped by the protoplanetary disk from their original resonant values. As shown above, eccentricity pumping during late-time divergent crossing of resonances can populate this area to the upper right in Figure 10.

3. WILL TIDES REMOVE RESIDUAL ECCENTRICITY?

The eccentricities shown in Figure 10 represent those at the end of the planetary assembly phase, i.e. they reflect the outcome of the dynamical interactions which produced the observed planetary system. While it would be very informative to probe these distributions directly, we must account for the fact that these planets lie close to their host stars and thus the distribution of eccentricities may be substantially modified by tides. We focus here

on tidal dissipation in the planet itself, as our interest in small planets suggests that tides raised in the star will not be important.

A calculation of tidal effects from first principles is quite uncertain as there are many potentially contributing physical effects (Ogilvie 2014). A common approach to average over the various possibilities is to adopt a parameterised tidal strength, most commonly in terms of the ‘Tidal Q’, following Goldreich & Soter (1966). We adopt a version of this model from Jackson et al. (2008), in which the eccentricity of an isolated planet damps as $e(t) = e(0)\exp(-t/\tau)$, where

$$\tau = \frac{4}{63} Q' \frac{M_p a_0^{13/2}}{R_p^5 (GM_*^3)^{1/2}} \quad (2)$$

and where Q' is a measure of the dissipation strength, a_0 is the semi-major axis of the planet, R_p and M_p are the planetary radius and mass, and M_* is the host star mass. When we adopt common values (discussed further below) for these numbers

$$\tau_e = 73 \text{ Gyrs} \left(\frac{Q'}{10^3} \frac{M_p}{M_\oplus} \right) \left(\frac{R_\oplus}{R_p} \right)^5 \left(\frac{M_\odot}{M_*} \right)^{1/2} \left(\frac{a_0}{0.1 \text{ AU}} \right)^{13/2} \quad (3)$$

There is still some ambiguity in this expression, as we must specify a mass-radius relation for the planet.

We assume two broad classes of planet in this sample. We assume that all planets with mass $< 10M_\oplus$ are rocky, with mass radius-relation given by the Silicate equation of state from Zeng et al. (2021). For planets with mass $> 10M_\oplus$, we assume the mass-radius relationship from Lopez & Fortney (2014), assuming a 1% Hydrogen mass fraction and the high irradiation case. For the rocky planets, we assume $Q' = 10^3$. Although the empirical value of Q' estimated for Earth is significantly smaller, it is believed that this is dominated by ‘pelagic’ processes in the oceans, which are likely to be absent in such hot planets as discussed here. We adopt the larger value of Q' , more characteristic of dry, rocky planets, as calibrated by estimates for Mars and the elastic component of Earth’s response (Lainey 2016). For the more massive planets, with Hydrogen envelopes, we adopt $Q' = 10^4$ for this, as estimated for Neptune (Banfield & Murray 1992).

With the adoption of this model, we can assess how likely it is that the planets in our sample have had their eccentricities damped by tides. Figure 11 shows the planets from our simulations plotted in semi-major axis and mass, compared to contours for which $\tau = 5$ Gyr in the two tidal models we consider here. This plot suggests that many of the planets with orbital periods < 7 days may expect to be circularised, while those at longer periods should retain their primordial eccentricities.

We incorporate the above tidal model into our final eccentricity estimates for the simulated systems. To zeroth order, each planet will experience an exponential damping of the eccentricity on the timescale τ_e . As demonstrated by the distribution in Figure 11, the innermost planets in many of these systems will experience circularisation, although the planets exterior to this region should retain their eccentricities. The matter is further complicated by the fact that many of these planets are in close, compact, systems and will also experience mu-

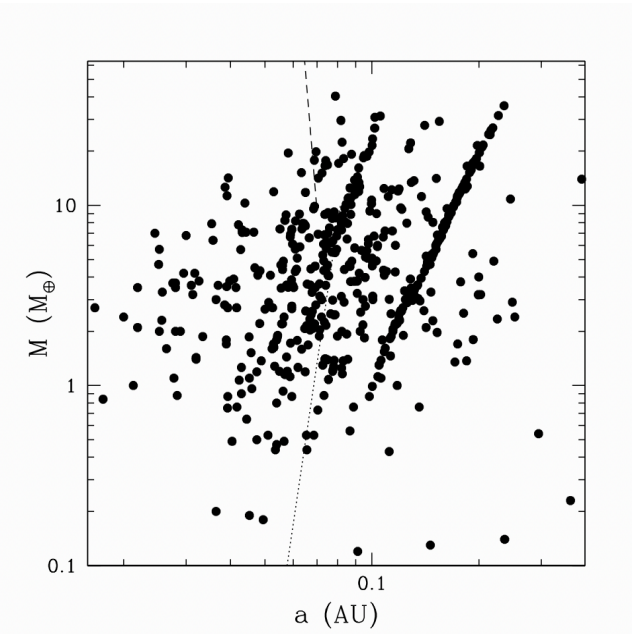


FIG. 11.— The solid points show the locations of the planets at the end of our simulations. The diagonal structure represents the locus of the outermost planets in the majority of the systems, and represents the mass-dependance of the freeze-out time (and hence the freeze-out location) from the late outward migration. The dotted curve represents a tidal dissipation time of 1 Gyr, assuming the model in the text with $Q' = 10^3$ and a mass radius relation at fixed (Earth-like) density. This is assumed to hold for $< 10M_\oplus$. The dashed line represents the same criterion, but for Super-Neptune, with a radius fixed at $4R_\oplus$ and $Q' = 10^4$. Within this model, the critical period for tidal circularisation is ~ 8 days.

tual gravitational interactions, which can transfer angular momentum between the planets, meaning that the eccentricities will evolve for the system as a whole, either in the case of secular interactions (Adams & Laughlin 2006; Greenberg & Van Laerhoven 2011; Hansen & Murray 2015; Pu & Lai 2019) or in the case of mean motion resonant interactions (Lithwick & Wu 2012; Batygin & Morbidelli 2013).

The latter is particularly important as the best information of eccentricities comes from transit time variations, which are most sensitive close to resonance. We incorporate our tidal evolution model above into the expression from Lithwick & Wu (2012) for the evolution of the separation Δ between two neighboring planets, assuming the tides are dominated by the inner planet.

$$\Delta_{\text{mig}} = 0.0024 \frac{\gamma}{Q'^{1/3}} \left(\frac{10M_\oplus}{M_1} \right)^{1/3} \left(\frac{R_1}{R_\oplus} \right)^{5/3} \left(\frac{a_1}{0.1 \text{ AU}} \right)^{-13/6} \quad (4)$$

and $\gamma = (2f_1\beta(1+\beta))^{1/3}$, $\beta = m_2/m_1\sqrt{a_2/a_1}$, f_1 is a constant associated with the particular resonance (given in Lithwick & Wu (2012)), and M_1, R_1 are the mass and radius of the inner planet (with M_2 the mass of the outer planet). Proximity to resonance implies a forced eccentricity that persists even after the free eccentricity is damped, which is then included.

Figure 12 shows the distribution of final planetary eccentricities in our model, both before (upper panel) and after (lower panel) the incorporation of tidal evolution. While there is a significant population of planets

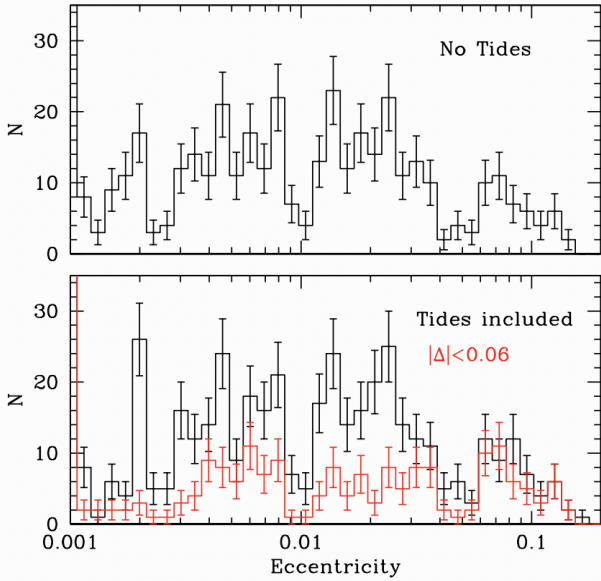


FIG. 12.— The upper panel shows the distribution of eccentricities that emerge from our final population of simulated planetary systems, without any correction for tidal effects. The black histogram in the lower panel shows the same distribution after it has been damped by tides using the model described in the text. The red histogram shows the same but only for planets that lie in a pair with $|\Delta| < 0.06$.

with very low eccentricities, there are also planets with $e > 0.1$. These are mostly systems that remain in resonance even after the dissipation of the gaseous disk. There is also a substantial population of planets with eccentricities in the range 0.01–0.1, which are well wide of resonance. Overall, $\sim 30\%$ of the simulated planets have $e > 0.01$ (even after correcting for tides).

The red histogram in the lower panel shows eccentricities only for those planets in pairs with $|\Delta| < 0.06$. Much of the information about observed eccentricities is gleaned from TTV, which favour small $|\Delta|$. The fraction of the red population that lie $e > 0.01$ is 46%, suggesting that measurements from TTV may be biased towards larger eccentricities than the overall population.

3.1. Inclinations

Deviations from coplanarity (i.e. inclinations relative to the Laplace plane of the system) can also be a measure of dynamical excitation. Our simulations were designed to measure evolution in a protoplanetary disk and so initial planetary inclinations were chosen with a dispersion of only 0.1° . Any significant variation from this would be a sign of dynamical heating.

Figure 13 shows the distribution of orbital inclinations relative to the plane of the original protoplanetary disk, at the end of our simulations. The bulk of the distribution remains at inclinations $< 0.1^\circ$. However, there is a tail that extends up to 10° . The overall distributions can be roughly fit with two different Rayleigh distributions – a low inclination one with dispersion $\sim 0.04^\circ$ and a second with a dispersion $\sim 1^\circ$, which is similar to the value inferred from fitting to Kepler multi-planet systems (Fang & Margot 2012; Xie et al. 2016; Van Eylen et al. 2019; Mills et al. 2019). The higher inclination

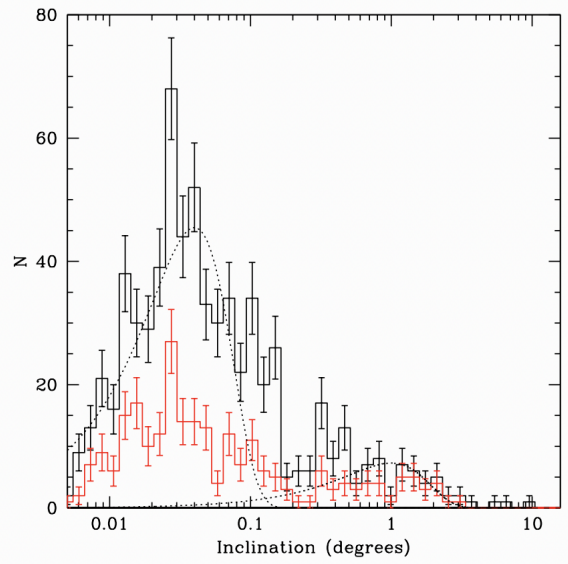


FIG. 13.— The black histogram shows the distribution of final inclinations for our simulated planets. The red histogram shows the subset which lie in pairs with $|\Delta| < 0.06$. The two dotted curves indicate Rayleigh distributions with dispersions of 0.04° and 1° respectively.

group corresponds to $\sim 16\%$ of the total population and also tend to be found within $|\Delta| < 0.06$, as can be seen from the comparison of the red and black histograms in Figure 13. This comparison is motivated by suggestions (He et al. 2019) that the observed excess of planets near mean motion resonance may be a consequence of a reduced inclination dispersion for planets in such configurations. Our results do not support this hypothesis – indeed, they go in the other direction. A larger fraction of the low inclination systems are removed with this Δ cut.

This higher inclination population are found in systems in which a pair received sufficient eccentricity excitation to undergo orbit crossing. Such pairs rapidly become dynamically unstable, resulting in planetary scattering and eventually collisions.

An example of such behaviour is shown in Figure 14. This shows an analogue of the five planet system Kepler-296. The system migrates inward as expected, but the third and fourth planets eventually collide (at 0.3 Myr) which generates an initial spike in the inclination of about 1° . This is amplified immediately afterwards, as the system establishes a new resonant chain. The end result of this shake-out is that the second and third planets move from a 3:2 resonance to a 5:3 second-order resonance, along with an exterior 3:2 resonance between the third and fourth planets (post collision – the new third planet is the sum of the original third and fourth planets). The fact that the system locks into a second order resonance means that the inclinations also adjust, as part of the resonance locking. There is also some late-time adjustment in the inclinations associated with the breaking of the chains as well.

4. COMPARING TO THE OBSERVATIONS

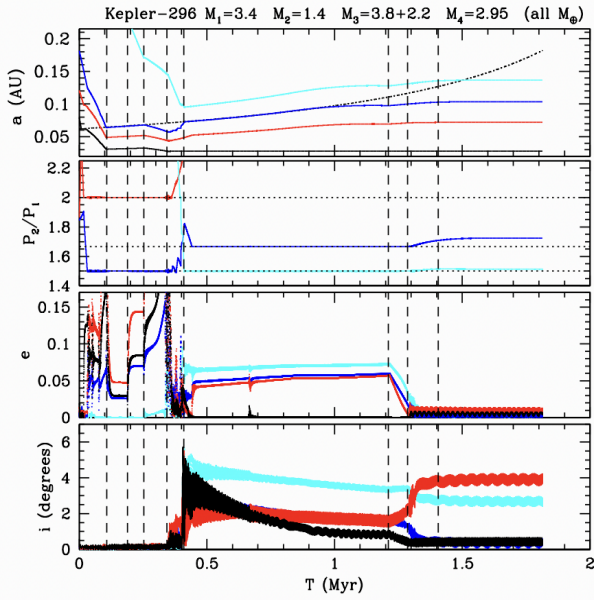


FIG. 14.— The upper panel shows the semi-major axis evolution of the four surviving planets. The second panel shows the evolution of the period ratios. The third panel shows the evolution of the eccentricities and the bottom panel shows the evolution of the planetary inclinations. The final third planet experiences a collision at 0.3 Myr, which generates the first increase in the inclinations.

We have quantified the level of residual dynamical excitation to be expected from the simulated systems in our simulated planetary systems. In this section, we compare these results to what is known about the observed compact planetary systems that motivated this model.

4.1. Free Eccentricities

The statistical distribution of eccentricities and inclinations of planetary orbits can be measured via the observation of transit durations, when allied with accurate characterisation of the host star dimensions. The application of this technique to the Kepler systems with multiple transiting planets (Xie et al. 2016; Van Eylen et al. 2019; Mills et al. 2019; Sagear & Ballard 2023; Gilbert et al. 2025) suggests low eccentricities, with varying analyses placing the mean eccentricity in the range $\sim 0.01\text{--}0.05$.

The best constraints on remnant eccentricities come from the observations of transit timing variations (Agol et al. 2005; Holman & Murray 2005; Fabrycky et al. 2012; Lithwick et al. 2012; Nesvorný et al. 2012; Mazeh et al. 2013; Steffen et al. 2013; Xie 2014; Hadden & Lithwick 2017; Jontof-Hutter et al. 2021), wherein the presence of nearby companions induce a precession of each planetary orbit. This, in turn, leads to variations in the time of transit, which can be measured. This method is most sensitive to pairs that are close to mean motion resonances, and allows for the detection of small, but non-zero, remnant free eccentricities in a significant sample of transiting systems (Hadden & Lithwick 2014, 2017; Jontof-Hutter et al. 2021). This provides a direct measure of the level of remnant dynamical excitation, which can be used to test our models. Measurement of eccentricity is somewhat degenerate with planetary mass,

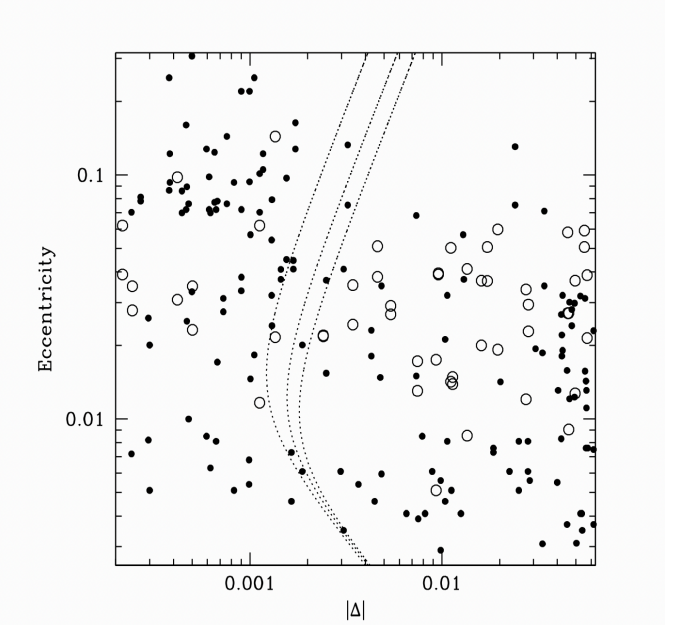


FIG. 15.— The filled circles represent the eccentricities of our simulated sample, after correction for tidal evolution. The large open circles are the estimated eccentricities for each planet in Table 17 of Jontof-Hutter et al. (2021), which are systems whose posterior measured distributions are inconsistent with circular. The dotted lines are the same as in Figure 10, roughly delineating the boundary between resonant (to the left) and non-resonant (to the right).

however, and so we restrict our observational sample to the systems in Table 17 of Jontof-Hutter et al. (2021), whose posterior distributions of measured eccentricities are inconsistent with zero. Figure 15 shows the central measured values of these systems, compared to the eccentricities shown in Figure 10, once again measured as a function of $|\Delta|$ – the proximity to the nearest first order commensurability.

The observed points are plotted without error bars because the goal of this comparison is not to compare individual systems, but to indicate that the remnant eccentricities in our model are of the same order as estimated for the observed samples, and also match the distribution in the Δ –eccentricity plane. The observational sample also contains many systems with similar estimated amplitudes whose posterior are also consistent with zero – and so are not plotted here – and so the presence of many simulated systems in the lower half of the plot are also consistent with observations.

Observations have also noted a trend with mass, in the sense that more massive systems have lower mean eccentricity (Hadden & Lithwick 2014). Figure 16 shows the eccentricity as a function of planet mass at the end of our simulations. Hadden & Lithwick (2014) noted that the eccentricity inferred from TTV was smaller in pairs of planets with mass $> 2.5R_{\oplus}$ than in planets with radii smaller than this. The precise conversion from radius to mass is uncertain, but we show (as red points) the approximate eccentricity dispersions inferred by Hadden & Lithwick (2014) as applied to planets either larger than $10M_{\oplus}$ or smaller. The results are in agreement with the simulations (it is worth emphasizing the red points are not fit to the black points, but taken from the observa-

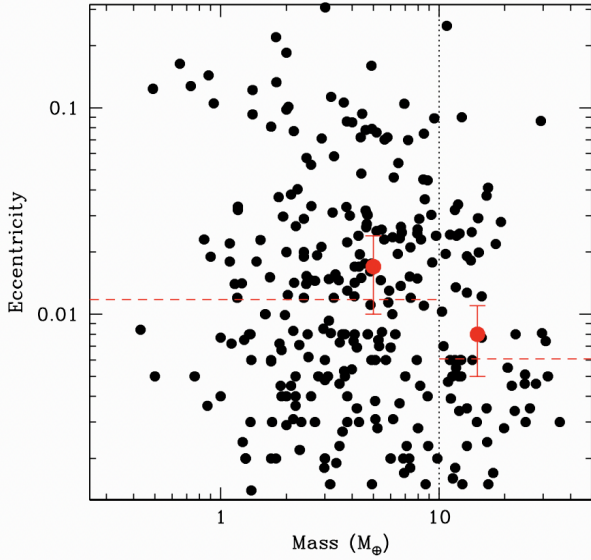


FIG. 16.— The black points show the eccentricity as a function of mass for planets with finite eccentricity at the end of our simulations. The two red points show the values inferred by Hadden & Lithwick (2014) for their high mass and low mass populations. We interpret these as representing populations either above or below the vertical dotted line at $10M_{\oplus}$. The horizontal red dashed lines represent the median value of the black points above and below this threshold.

tions).

There is also a weak mass trend with proximity to resonance. Those neighbouring pairs with $|\Delta| < 0.01$ have a mean total pair mass of $9.9 \pm 0.7M_{\oplus}$, and those with $0.01 < |\Delta| < 0.1$ have a mean total pair mass of $11.4 \pm 0.9M_{\oplus}$. However, wider pairs, with $|\Delta| > 0.1$, have a mean total mass of $15.2 \pm 0.8M_{\oplus}$. This trend is consistent with the consequence that more massive planets remain coupled to the disk for longer and can therefore diverge further, depending on the mass ratio. Observations (Leleu et al. 2024) also indicate a trend of increasing mass with increasing Δ .

4.2. Phase Information

Finite free eccentricities are also inferred as result of phase offsets in the mutual timing of the transits. For a system where the eccentricity is only due to the resonant forcing, the resonant pair should exhibit only small amplitude librations about the libration center, and this results in an expectation of alignment between the transit conjunction and mean transit configuration (Lithwick et al. 2012; Choksi & Chiang 2023). As the free eccentricity increases, the amplitude of this libration increases and the range of phase offset grows, before eventually entering circulation.

We have examined the transit timing of pairs in our simulated systems with $0.005 < \Delta < 0.1$, and calculated the transit phase as described in Choksi & Chiang (2023). In each case, we have measured the transit phase of the pair with and without the presence of other planets in the system, as the simple model used to calculate the phase (Lithwick et al. 2012; Choksi & Chiang 2023) is founded on the two planet model, which can be-

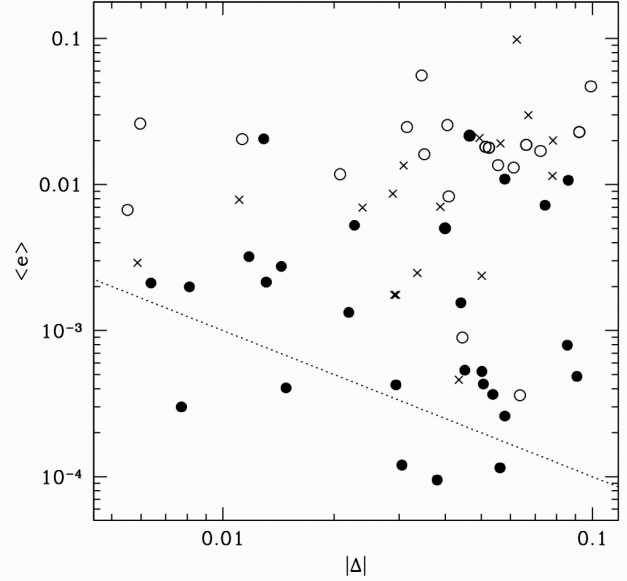


FIG. 17.— We plot each neighbouring pair with a symbol that indicates whether the TTV phase of the inner member of the pair librates (open symbol), circulates (filled symbol) or violates the assumptions (crosses) under which the equations in Choksi & Chiang (2023) are derived – which essentially means that it has not undergone the resonant fixed point bifurcation as discussed in Murray & Dermott (2000) chapter 8.

come significantly more complicated in multiplanet systems where additional sources of precession, and the influence of neighbouring resonances, can affect the phase (see Li et al. (2025) for a similar discussion). Simulated results can show complex phase evolutions on timescales that are not captured by the limited span of the observations. As a result, we classify systems as librating simply if their phases explore a limited range $< 90^\circ$, and as circulating if the phases explore a larger range. We have also calculated the phases using only the properties of the pair in question, and in the case where the pair is embedded within the full planetary system from which it is drawn.

Figure 17 classifies the simulated systems in terms of the behaviour of their transit phases. We plot Δ versus mean eccentricity ($\langle e \rangle = \frac{1}{2}(e_1 + e_2)$) for each relevant pair. Systems plotted as solid points exhibit libration of the transit phase both when we simulate only the neighbouring pair and also when all the system planets are included.

Open circles show systems that exhibit transit phase circulation, again in both the case of the isolated pair and with all the planets in the system. The systems plotted as crosses exhibit libration of the transit phase for the isolated two planet system, but show phase circulation when the perturbations from the other planets are included.

Overall, the pattern of points in Figure 17 correspond to expectations. Systems with $|\Delta| \sim 0.01$, or larger, still exhibit small amplitude libration if their eccentricities are small enough. This is the expected behaviour for systems that evolve away from resonance while eccentricity damping continues to operate. It is also the

behaviour expected from resonant repulsion as the forced eccentricity dies away as the pair diverges (Lithwick & Wu 2012; Batygin & Morbidelli 2013; Choksi & Chiang 2020). The dotted line in Figure 17 shows the level of eccentricity consistent with resonance as a function of Δ .

However, if a diverging pair crosses a resonance, it experiences a kick to both the eccentricity and the TTV phase. This elevates the system to larger eccentricity at fixed Δ , moving it towards the upper right in Figure 17. Indeed, this is where we find the open points, indicative of circulating Φ_{TTV} .

4.3. Three Body Resonances

All of the planetary systems in our simulations form resonant chains, and so they also show libration in a variety of three-body resonances, as can be seen from the corresponding panels in Figures 3–6. These panels also show that most of these resonant angles begin circulating as soon as the two body resonance locks are broken. However, as they diverge, many of the systems remain closer to their three-body commensurabilities than their two body ones.

In fact, Cerioni et al. (2022) find evidence that the Kepler planetary systems show a greater preference for three body commensurabilities than for two body commensurabilities, which they interpret as potential evidence that three body resonance capture plays an important part in the migration of compact planetary systems. The weakness of such resonances would therefore require that eccentricity excitation remains low during the migration process (Charalambous et al. 2018; Goldberg & Batygin 2021). Our model provides an alternative route to this excess of proximity to three-body resonance.

Figure 18 shows the results from our simulations, composed of all the three-body neighbouring combinations from surviving three, four and five body systems. The red curves represent the possible three body commensurabilities that intersect combinations of the 4:3, 3:2 and 2:1 mean motion resonances. Cerioni et al. (2022) highlighted three particular combinations, which we show as solid lines. They also restricted their domain of interest to compact systems, wherein all neighbour period ratios < 1.7 . To compare our results to theirs, we can quantify the proximity to a three body resonance with

$$\Delta' = k_i \frac{P_2}{P_1} + k_{i+2} \frac{P_2}{P_3} - k_{i+1}. \quad (5)$$

Within the domain of interest of Cerioni et al. (2022), we find that 10% of our simulations have $|\Delta'| < 0.01$, while the Kepler sample shows a fraction of 19% with the same cuts.¹ However, if we extend the range of period ratios up to 3, we see that $\sim 40\%$ of the points shown in Figure 18 lie within $|\Delta'| < 0.005$ of a three body resonance. This is artificially high, because it does not yet account for probability of observing a transit. If we model the observability of each system from random inclinations (and assume it is detected if geometrically possible), then this fraction drops to 26% (many of the three-body resonances are wide of the 2:1 MMR, making them more susceptible to geometric selection effects). However, extending the

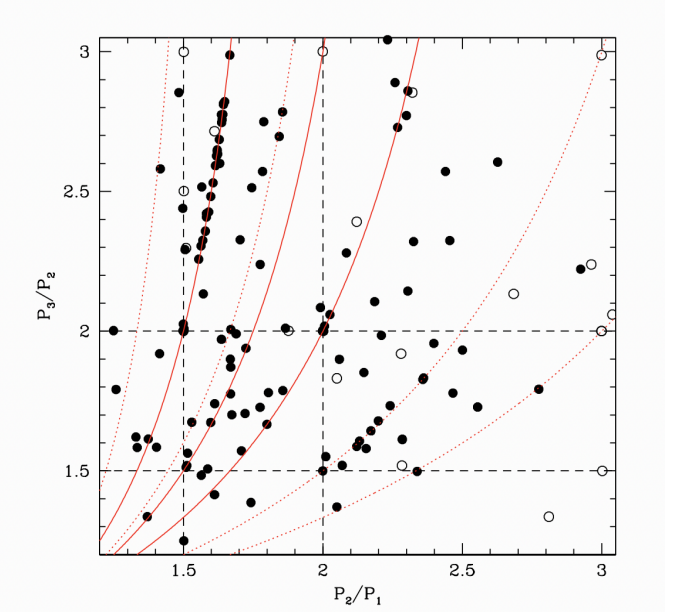


FIG. 18.— The filled circles show the period ratio combinations for the neighbouring triples produced by our simulations. Open circles show triples produced from a four planet system in which one of the planets is missed (not transiting). There are few of these shown, because many fall above or to the right of the domain presented here. The red curves represent all of the three body commensurabilities that can be produced by combining 4:3, 3:2 and 2:1 mean motion resonances. The solid curves represent the three combinations highlighted by Cerioni et al. (2022). The horizontal and vertical dashed lines indicate the common two body commensurabilities.

bounds of the observational sample shows that only 7% of the observed systems meet this criterion.

Thus, our simulations are consistent with the statistics of Cerioni et al. (2022) for compact systems, but that we see an excess of three-body commensurabilities in wider spaced systems at the end of our simulations.

4.4. Dynamical Stability

One important conceptual difference between origin models concerns how early in a planetary system lifetime is the final dynamical configuration set. The model described here falls into the broad class wherein migration is driven by interaction with the protoplanetary disk, and the incorporation of a more realistic inner boundary condition results in a widespread dynamical disruption of resonant chains during the late stages of the protoplanetary disk dispersion. As a result, the final dynamical configurations are largely in place at the end of the disk phase (within a few Myr). Although further dynamical evolution is not excluded, the comparisons above indicate that the final configurations of the simulated systems at the end of the disk evolution phase are similar to the observed configurations.

The final configurations in our simulations are also broadly consistent with long-term dynamical stability. An illustration of this is shown in Figure 19, which summarises the final separations of the neighbouring pairs in our simulations, when measured in terms of mutual Hill

¹ We should note that our observed sample is not exactly the same as Cerioni et al. (2022), who drew their sample from an internet archive and thus may exhibit a variety of selection effects.

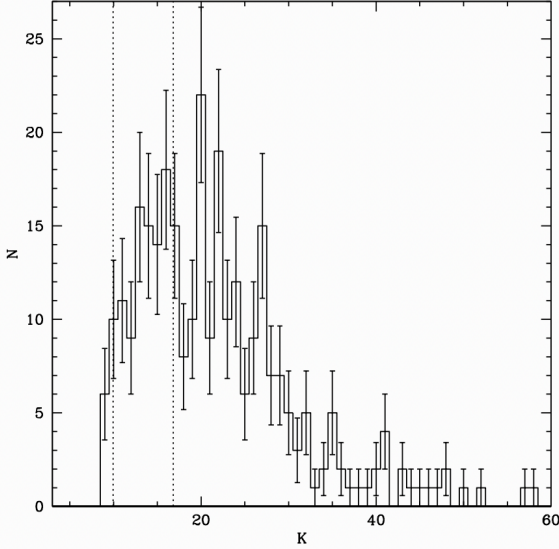


FIG. 19.— The histogram shows the spacing K of neighbouring pairs of planets in the final outputs of our simulations, expressed in mutual Hill radii. The two vertical dotted lines indicate the value that would apply for a pair of $10M_{\oplus}$ planets, in either a 3:2 or a 2:1 mean motion resonance.

radii. We define this separation as

$$K = \frac{(a_{i+1} - a_i)}{(a_{i+1} + a_i)/2} \left(\frac{M_{i+1} + M_i}{3} \right)^{-1/3} \quad (6)$$

where a_i and M_i are the semi-major axis and mass of planet i . The overall distribution peaks in the range $15 < K < 25$, which is well clear of the threshold of short term instability. The distribution is quite similar to the empirical determination from Pu & Wu (2015). The numerical stability simulations of Pu & Wu (2015) also suggest that the threshold for 50% stability will lie in the range $K \sim 10-12$, for levels of eccentricity excitation characteristic of our simulations, and for Gyr timescales. This suggests that there is no reason to expect wholesale dynamical evolution of these systems on longer timescales (absent additional perturbations).

As a result, our models suggest that the dynamical configurations of compact planetary systems are largely in place at the end of the protoplanetary disk phase, unlike other models (Izidoro et al. 2017, 2021) that generally require the systems at the end of the protoplanetary disk phase to undergo significant dynamical evolution on longer timescales to disrupt the resonant chains..

This appears to stand at odds with the recent claim from Dai et al. (2024), namely that the sample of planetary systems orbiting stars with ages < 100 Myr has a much higher frequency of near resonant planetary pairs ($70 \pm 15\%$) than the overall Kepler sample ($15.6 \pm 1.1\%$). To understand how our simulations compare to this observation, we re-examine the young sample from Dai et al. (2024). Of particular concern is the inclusion of planets that were initially detected from the Transit Timing Variations they induced in other planets. The amplitudes of TTV are widely known to be stronger for systems close to resonance (Agol et al. 2005) and so the

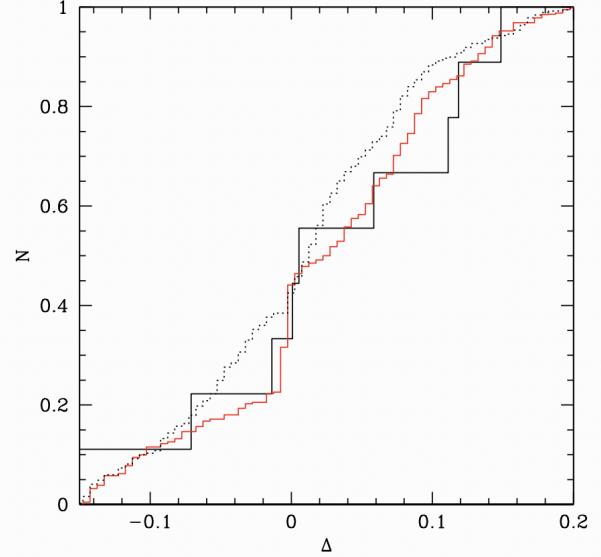


FIG. 20.— The solid histogram shows the distribution of Δ amongst the young sample in Dai et al. (2024), edited as discussed in the text. The red histogram is the corresponding distribution, over the same range in Δ , from the simulations presented here. The dotted histogram shows the distribution for the Kepler sample over the same range, subject to the same $P < 40$ days cut as in Figure 7.

inclusion of these systems biases the sample in the direction of near-resonant systems. The consequences of this selection effect are particularly severe for the youngest planet sample in Dai et al. (2024).

Thus, in our comparison, we exclude the two young planets (AU Mic d and TOI-1227c) detected in this way. We also include an additional planet (AU Mic e) that has been detected, in one of the observed systems, using radial velocities. Finally, Dai et al. (2024) cite an unpublished ephemeris for V 1298 Tau, so we use that from Feinstein et al. (2022). We also restrict ourselves to Δ calculated relative to first order resonances (Dai et al. (2024) include second order resonances) to be consistent with the other comparisons in this paper. With this revised young planet sample, we find 3/9 planetary pairs satisfy the Dai et al. (2024) criterion for proximity to resonance, namely $-0.015 < \Delta < 0.03$. This is a fraction of $33 \pm 19\%$, which is less than 1σ discrepant from the overall Kepler rate. If we had included the two planets detected by TTV, this would have risen to 6/11. The resulting distribution of Δ for our revision of this young sample is shown as the black solid histogram in Figure 20, and is compared with the distribution of Δ from our simulations (if restricted to the range $-0.15 < \Delta < 0.2$). We see that the shape of the Δ distribution around 0 is actually very similar, and closer than the corresponding distribution from the overall Kepler sample, shown as the dotted histogram.

Thus, viewed in terms of the distribution around $\Delta \sim 0$, our simulations match those of Dai et al. (2024) very well, in accord with new modelling in Hu et al. (private communication) which suggests most of this sample is near, but not in, resonance. There is one important

discrepancy though, in the sense that $\sim 44\%$ of the simulated neighbouring pairs have $|\Delta| > 0.2$, but there are no such systems in the Dai et al. (2024) young stellar sample. One interpretation of this comparison is that there is some room for later dynamical evolution to broaden the shape of the distribution around $\Delta \sim 0$ (to move from the red histogram to the dotted histogram in Figure 20) but that the amount of evolution expected is a lot less than suggested by Dai et al. (2024).

5. CONCLUSIONS

The residual level of dynamical excitation in compact exoplanet systems is a potentially powerful diagnostic of the mechanisms which determine the final state of the planetary system architectures. Here we have examined the level of excitation to be expected in the scenario outlined in Yu et al. (2023) and Hansen et al. (2024). The residual eccentricities in these systems are largely imposed during the final stage of protoplanetary disk clearing, as diverging pairs cross mean motion resonances, which results in a transient eccentricity kick to the system. The fact that most of the divergence occurs at late times also means that the eccentricities are incompletely damped, leaving a finite value after complete dissipation of the disk. We have demonstrated that the resulting residual eccentricities are consistent with the level observed in transiting planet systems, as measured through transit duration distributions and transit timing variations. We also reproduce the broad trend that more massive planets are less eccentric.

We have shown that the late stage divergence also results in most neighbouring pairs breaking free of resonant lock, resulting in only a small fraction of planets remaining in resonance. We find that the residual fraction of systems near strict commensurability is similar to that observed, although some details of the structure near $\Delta \sim 0$ are not reproduced. However, the distribution near $\Delta \sim 0$ is well matched to that of planetary systems that orbit young stars, although the current sample of the latter population does appear to lack the widest systems expected from the simulations.

Our broad conclusion from this comparison is that a model in which the stellar magnetic field sculpts the inner edge of the protoplanetary disk can explain the observed dynamical properties of compact extrasolar planet

architectures. Planetary migration in simple disk models, with a sharp density cutoff at the inner edge, results in long-lived resonant chains, but the problem is avoided if the models include the effect in which the stellar field diffuses into the disk and modifies the surface density profile. In this case, the magnetospheric rebound at late times leads to widespread divergent evolution and disruption of the resonant chains. This divergence and disruption also leaves behind a level of dynamical excitation that is comparable to that observed.

It is natural to compare these results to the currently fashionable paradigm in which the planets emerge from the protoplanetary disk in resonant chains, which only break up on longer timescales. These models either require an unknown additional source of eccentricity excitation (Li et al. 2025) or capture into very compact configurations of mean motion resonance (Izidoro et al. 2021), which do not correspond to the observed young planet configurations of Dai et al. (2024). In contrast, the magnetospheric rebound model presented here generates the broad features of the dynamical architecture at the end of protoplanetary disk phase without any selective editing to identify specific unstable subsets. As such, it does not require widespread dynamical instabilities on longer timescales. This does not preclude some level of additional dynamical evolution, but it reduces the need considerably, and may lessen the demands on some of the proposed mechanisms. Most importantly, it reproduces the remnant levels of eccentricity excitation observed through timing transit observations.

Data availability: The data underlying this article will be shared on reasonable request to the corresponding author.

The authors thank Nick Choksi & Fei Dai for comments on a preprint of this work. Y.H. was supported by the Jet Propulsion Laboratory, California Institute of Technology, under a contract with the National Aeronautics and Space Administration (80NM0018D0004). This research has made use of the NASA Exoplanet Archive, which is operated by the California Institute of Technology, under contract with the National Aeronautics and Space Administration under the Exoplanet Exploration Program. This research has made use of NASA's Astrophysics Data System Bibliographic Services.

REFERENCES

Adams F. C., Laughlin G., 2006, *ApJ*, 649, 1004
 Agol E., Steffen J., Sari R., Clarkson W., 2005, *MNRAS*, 359, 567
 Banfield D., Murray N., 1992, *Icarus*, 99, 390
 Batalha N. M., et al., 2013, *ApJS*, 204, 24
 Batygin K., Morbidelli A., 2013, *AJ*, 145, 1
 Becker J. C., Adams F. C., 2017, *MNRAS*, 468, 549
 Boley A. C., Morris M. A., Ford E. B., 2014, *ApJ*, 792, L27
 Borucki W. J., et al., 2010, *Science*, 327, 977
 Cerioni M., Beaugé C., Gallardo T., 2022, *MNRAS*, 513, 541
 Chambers J. E., 1999, *MNRAS*, 304, 793
 Chambers J. E., 2001, *Icarus*, 152, 205
 Charalambous C., Martí J. G., Beaugé C., Ramos X. S., 2018, *MNRAS*, 477, 1414
 Chatterjee S., Ford E. B., 2015, *ApJ*, 803, 33
 Chatterjee S., Tan J. C., 2015, *ApJ*, 798, L32
 Chen J., Kipping D., 2017, *ApJ*, 834, 17
 Chen J., Kipping D. M., 2018, *MNRAS*, 473, 2753
 Chiang E., Laughlin G., 2013, *MNRAS*, 431, 3444
 Choksi N., Chiang E., 2020, *MNRAS*, 495, 4192
 Choksi N., Chiang E., 2023, *MNRAS*, 522, 1914
 Coleman G. A. L., Nelson R. P., 2014, *MNRAS*, 445, 479
 Cossou C., Raymond S. N., Hersant F., Pierens A., 2014, *A&A*, 569, A56
 Coughlin J. L., et al., 2016, *ApJS*, 224, 12
 Cresswell P., Nelson R. P., 2006, *A&A*, 450, 833
 Dai F., et al., 2024, *AJ*, 168, 239
 Dawson R. I., Lee E. J., Chiang E., 2016, *ApJ*, 822, 54
 Delisle J. B., 2017, *A&A*, 605, A96
 Denham P., Naoz S., Hoang B.-M., Stephan A. P., Farr W. M., 2019, *MNRAS*, 482, 4146
 Fabrycky D. C., et al., 2012, *ApJ*, 750, 114
 Fabrycky D. C., et al., 2014, *ApJ*, 790, 146
 Fang J., Margot J.-L., 2012, *ApJ*, 761, 92
 Feinstein A. D., et al., 2022, *AJ*, 164, 110
 Fressin F., et al., 2013, *ApJ*, 766, 81
 Ghosh T., Chatterjee S., 2023, *ApJ*, 943, 8
 Gilbert G. J., Fabrycky D. C., 2020, *AJ*, 159, 281

Gilbert G. J., Petigura E. A., Entrican P. M., 2025, Proceedings of the National Academy of Science, 122, e2405295122

Goldberg M., Batygin K., 2021, AJ, 162, 16

Goldberg M., Batygin K., 2022, AJ, 163, 201

Goldreich P., Soter S., 1966, Icarus, 5, 375

Greenberg R., Van Laerhoven C., 2011, ApJ, 733, 8

Hadden S., Lithwick Y., 2014, ApJ, 787, 80

Hadden S., Lithwick Y., 2017, AJ, 154, 5

Hands T. O., Alexander R. D., 2016, MNRAS, 456, 4121

Hansen B. M. S., 2017, MNRAS, 467, 1531

Hansen B. M. S., Murray N., 2012, ApJ, 751, 158

Hansen B. M. S., Murray N., 2013, ApJ, 775, 53

Hansen B. M. S., Murray N., 2015, MNRAS, 448, 1044

Hansen B. M. S., Yu T.-Y., Hasegawa Y., 2024, The Open Journal of Astrophysics, 7, 61

He M. Y., Ford E. B., Ragozzine D., 2019, MNRAS, 490, 4575

Hellary P., Nelson R. P., 2012, MNRAS, 419, 2737

Holman M. J., Murray N. W., 2005, Science, 307, 1288

Huang C. X., Petrovich C., Deibert E., 2017, AJ, 153, 210

Ida S., Lin D. N. C., 2008, ApJ, 673, 487

Ida S., Lin D. N. C., 2010, ApJ, 719, 810

Izidoro A., Ogihara M., Raymond S. N., Morbidelli A., Pierens A., Bitsch B., Cossou C., Hersant F., 2017, MNRAS, 470, 1750

Izidoro A., Bitsch B., Raymond S. N., Johansen A., Morbidelli A., Lambrechts M., Jacobson S. A., 2021, A&A, 650, A152

Jackson B., Greenberg R., Barnes R., 2008, ApJ, 678, 1396

Jontof-Hutter D., Wolfgang A., Ford E. B., Lissauer J. J., Fabrycky D. C., Rowe J. F., 2021, AJ, 161, 246

Lainey V., 2016, Celestial Mechanics and Dynamical Astronomy, 126, 145

Laskar J., 1997, A&A, 317, L75

Leleu A., et al., 2024, A&A, 687, L1

Li G., Naoz S., Valsecchi F., Johnson J. A., Rasio F. A., 2014, ApJ, 794, 131

Li R., Chiang E., Choksi N., Dai F., 2025, AJ, 169, 323

Lin J., Dudiak I., Hadden S., Tamayo D., 2024, arXiv e-prints, p. arXiv:2412.12415

Lissauer J. J., et al., 2011, ApJS, 197, 8

Lissauer J. J., Rowe J. F., Jontof-Hutter D., Fabrycky D. C., Ford E. B., Ragozzine D., Steffen J. H., Nizam K. M., 2023, arXiv e-prints, p. arXiv:2311.00238

Lithwick Y., Wu Y., 2012, ApJ, 756, L11

Lithwick Y., Xie J., Wu Y., 2012, ApJ, 761, 122

Liu B., Ormel C. W., Lin D. N. C., 2017, A&A, 601, A15

Lopez E. D., Fortney J. J., 2014, ApJ, 792, 1

Masset F., Snellgrove M., 2001, MNRAS, 320, L55

Matsumoto Y., Ogihara M., 2020, ApJ, 893, 43

Mazeh T., et al., 2013, ApJS, 208, 16

Mills S. M., Howard A. W., Petigura E. A., Fulton B. J., Isaacson H., Weiss L. M., 2019, AJ, 157, 198

Murray C. D., Dermott S. F., 2000, Solar System Dynamics, doi:10.1017/CBO9781139174817.

Mustill A. J., Wyatt M. C., 2011, MNRAS, 413, 554

Mustill A. J., Davies M. B., Johansen A., 2017, MNRAS, 468, 3000

Nesvorný D., Kipping D. M., Buchhavet L. A., Bakos G. Á., Hartman J., Schmitt A. R., 2012, Science, 336, 1133

Ogilvie G. I., 2014, ARA&A, 52, 171

Petigura E. A., Howard A. W., Marcy G. W., 2013, Proceedings of the National Academy of Science, 110, 19273

Poon S. T. S., Nelson R. P., 2020, MNRAS, 498, 5166

Poon S. T. S., Nelson R. P., Jacobson S. A., Morbidelli A., 2020, MNRAS, 491, 5595

Pu B., Lai D., 2019, MNRAS, 488, 3568

Pu B., Lai D., 2021, MNRAS, 508, 597

Pu B., Wu Y., 2015, ApJ, 807, 44

Sagear S., Ballard S., 2023, Proceedings of the National Academy of Science, 120, e2217398120

Shariat C., Hasegawa Y., Hansen B. M. S., Yu T. Y. M., Hu R., 2024, ApJ, 964, L13

Steffen J. H., et al., 2013, MNRAS, 428, 1077

Terquem C., Papaloizou J. C. B., 2007, ApJ, 654, 1110

Terquem C., Papaloizou J. C. B., 2019, MNRAS, 482, 530

Thompson S. E., et al., 2018, ApJS, 235, 38

Van Eylen V., et al., 2019, AJ, 157, 61

Wang X., Zhou L.-Y., Beaugé C., 2024, A&A, 687, A266

Wu Y., Malhotra R., Lithwick Y., 2024, ApJ, 971, 5

Xie J.-W., 2014, ApJS, 210, 25

Xie J.-W., et al., 2016, Proceedings of the National Academy of Science, 113, 11431

Yu T. Y. M., Hansen B., Hasegawa Y., 2023, MNRAS, 523, 3569

Zeng L., et al., 2021, ApJ, 923, 247

This paper was built using the Open Journal of Astrophysics L^AT_EX template. The OJA is a journal which

provides fast and easy peer review for new papers in the **astro-ph** section of the arXiv, making the reviewing process simpler for authors and referees alike. Learn more at <http://astro.theoj.org>.